This is a post-print version of the article. The final published version can be found on Science Robotics website.

Manuscript Template

Title

Millimeter-Scale Flexible Robots with Programmable Three-Dimensional Magnetization and Motions

Authors

Tianqi Xu, Jiachen Zhang, Mohammad Salehizadeh, Onaizah Onaizah, and Eric Diller

Affiliations

Department of Mechanical and Industrial Engineering, Microrobotics Lab, University of Toronto, 5 King's College Rd., Toronto, Ontario, Canada, M5S 3G8

Abstract

Flexible magnetic small-scale robots use patterned magnetization to achieve fast transformation into complex three-dimensional (3D) shapes, and thereby achieve locomotion capabilities and functions. These capabilities address current challenges for microrobots in drug delivery, object manipulation, and minimally invasive procedures. However, possible microrobot designs are limited by the existing methods for patterning magnetic particles in flexible materials. Here, we report a method for patterning hard magnetic microparticles in an elastomer matrix. This method, based on UV-lithography, uses controlled reorientation of magnetic particles and selective exposure to UV light to encode magnetic particles in planar materials with arbitrary 3D orientation with a geometrical feature size as small as 100 µm. Multiple planar microrobots with various sizes, different geometries, and arbitrary magnetization profiles can be fabricated from a single precursor in one process. Moreover, a 3D magnetization profile allows higher-order and multi-axis bending, large-angle bending, and combined bending and torsion in one sheet of polymer, creating previously unachievable shape changes and micro-robotic locomotion mechanisms such as multi-arm power grasping and multi-legged paddle-crawling. A physics-based model is also presented as a design tool to predict the shape changes under magnetic actuation.

Summary

New types of flexible microrobots are enabled by patterning discrete 3D magnetization.

Introduction

Millimeter- and micrometer-scale robots have a growing number of potential applications in healthcare, bioengineering, and microfactories (*1–4*). Because such microrobots are subject to microscale physics and dynamics, the actuation mechanisms commonly used differ from those for traditional large-scale robots. Common microrobot actuation mechanisms use piezoelectric actuators (*5*, *6*), stimuli-responsive materials (*7–9*), chemical fuel (*10*), acoustic radiation force driving (*11*, *12*), and optothermal trapping (*13*, *14*). These mechanisms have been used to design various types of artificial muscles and self-folding structures, demonstrating their utility for high-precision applications despite the compact designs. However, there is a trade-off among response speed, ease of access and control, and available shapes of transformation. Thus, untethered microrobots that have programmable three-dimensional deformation and instantaneous response are still not fully achieved.

Magnetic actuators are distinguished for their fast response to input signals and the ability to be controlled wirelessly in confined spaces. In addition, safe robot-human interaction and lower cost make them ideal tools for in vivo disease diagnosis and treatment (*15–17*). To date, most studies focused on rigid magnetic microrobots. Although these robots have no more than five actuated degrees of freedom under a magnetic field, their geometries are designed to convert simple translation and rotation into functional motions for applications such as targeted drug delivery (*17–20*), cell culture (*21*), assisted fertilization (*22*), and non-invasive medical intervention inside the vascular system (*23*). However, as these microrobots are confined by the simple uniform distribution of magnetic moments in a rigid body, they lack the ability to form internal deformation, which is necessary for sophisticated motions such as grasping and crawling. To overcome these limitations, flexible magnetic materials which have programmable morphologies can be used (*24*).

Programmable morphologies of flexible magnetic materials are realized by patterning magnetic particles in a polymer composite. The magnetic particles can either be magnetically soft, not retaining their magnetization when an applied magnetic field is removed, or magnetically hard, retaining some magnetization. Soft magnetic particles can be synthesized at the nanometer size (*25*) and can be lithographically patterned into hydrogel sheets (*26*, *27*) or other artificial composites (*28*). The morphology of the hydrogel sheets is programmed by the formation of aligned soft magnetic nanoparticle chains, which function as preferred magnetic axes as well as components to reinforce material rigidity. In comparison, hard magnetic particles can be synthesized only at micrometer or larger size, but the remanent magnetization of pre-magnetized particles enables more sophisticated capabilities such as complex locomotion modes (*29–31*), object manipulation and assembly (*32–34*), and fast 3D transformation (*35*). Different techniques for patterning hard magnetic particles have been used to realize the heterogeneous magnetization and thus the independent addressability to different parts with a global actuating magnetic field (Table 1).

However, previous patterning methods still cannot achieve all types of magnetic torque-induced deformations because the ability to precisely pattern discrete 3D magnetization in planar soft materials has not been shown. Such capability would enable new types of sophisticated micro-robotic devices with programmable shape changes. For example, we show multi-arm structures that can transform into a hollow sphere under a static magnetic field. To date, microrobots that have discrete 3D magnetization profiles and patterned shapes below centimeter size can be fabricated only by manual microassembly of magnetic components, but the cost and difficulty rise dramatically in association with size, number of parts, and magnetization complexity.

Here, we report a UV-lithography-based method to encode 3D magnetization in planar flexible composites at the sub-millimeter scale. Similar to photolithography-based patterning technique for soft magnetic particles (*26–28*), in this method we precisely reorient pre-magnetized permanent magnetic particles and then selectively cure UV resin to pattern the local magnetization. Multiple microrobots that have different geometries and 3D magnetization profiles can be

fabricated from the same precursor in a single process. We achieve a geometrical feature size as small as 100 μm × 100 μm and precise magnetization feature size as small as 250 μm × 250 μm on an 80 μm thick UV resin layer. Using this method, we fabricate millimeter-scale structures that exhibit higher-order and multi-axis deformation, large-angle bending, or combined bending and torsion. We also present new micro-robotic capabilities enabled by this technique and provide a model to predict the shape changes which can be used as a design tool.

Table 1. Capabilities of major existing methods to pattern magnetic particles

Method	Magnet type	Shape of media *	Template or mold required	States of magnetization †
Electrodeposition of magnetic particles on lithographically printed microstructures (*18*, *21*, *22*)	Soft	3D	No	N/A
Lithographic patterning of magnetic nanoparticles (*26–28*)	Soft	2D	No	Discrete, 3D
Magnetic particles linked by DNA (*36*)	Soft	N/A	No	Discrete, 1D
Microassembly of magnetic components (*33*, *34*, *37*)	Hard	3D	Yes	Discrete, 3D
Magnetic recording technology (*38*)	Hard	2D	No	Discrete, 1D
Template-aided magnetizing (*29–31*)	Hard	2D	Yes	Continuum, 3D
3D printing of ferromagnetic domains (*35*)	Hard	3D	No	Discrete, 2D
This work	Hard	2D	No	Discrete, 3D

* Shape of media refers to the structure of the composite materials in which the magnetic particles are dispersed. 2D refers to planar structures while 3D refers to solid three-dimensional structures.
† States of magnetization is defined as degrees of freedom related to the orientation of hard magnetic particles or preferred magnetic axes of soft magnetic particles in each area.
1D: only binary magnetization can be patterned, e.g. longitudinal or perpendicular recording in a hard disk drive.
2D: direction of magnetization in each layer is restricted to a single plane.
3D: magnetization in each layer can be patterned in arbitrary direction.
Discrete: magnetization in each area is independent of adjacent areas.
Continuum: magnetization in each area cannot have sudden changes with respect to adjacent areas.

Results

Patterning discrete 3D magnetization

In this work, discrete means local magnetization can have sudden changes with respect to adjacent areas. 3D refers to the degrees of freedom related to the orientation of integrated magnetic particles. The ability to precisely program discrete 3D magnetization in flexible materials can enable planar actuators that have arbitrary distribution of magnetic torque. The desired magnetic torque distribution, expressed as a function of location, can be directly mapped to the magnetization profile of the sheet if the size of each magnetization area is sufficiently small. In addition to precise patterning, discrete 3D magnetization can enhance the performance of magnetic actuators and introduce new designs. For simple bending or torsion, local magnetization can be programmed to maintain 90° with respect to the actuating field to maximize deformation, making it possible for millimeter-scale actuators to have large deformations under a weaker actuating magnetic field. New shape changes are enabled by the capability to pattern highly discontinuous magnetization profiles in complex geometries. For example, we show planar structures that have multiple unparalleled bending axes and large bending angles (as large as 180°) under a static magnetic field.

Fig. 1A shows the physical apparatus for patterning 3D discrete magnetization in planar UV-curable materials. The materials in the substrate are prepared by mixing pre-magnetized hard magnetic particles with flexible UV resin. With the 3-axis Hall effect sensor providing feedback data, the cube permanent magnet under the substrate can generate a magnetic field to precisely

reorient all the magnetic particles included in the UV resin. After particle reorientation, the DLP (Digital Light Processing) projector emits UV light on selected regions of the substrate, which initiates polymerization and freezes the magnetic particles within those regions. This automated two-step patterning procedure can be optionally repeated depending on the complexity of the actuator design. Movie S1 shows the automated fabrication process. Fig. 1B shows the influence of magnetic particle concentration on UV penetration depth. As the mass ratio approaches 1.5:1, the magnetic slurry becomes highly viscous and the difficulty of reorienting the particles increases dramatically. Therefore, we recommend the mass ratio of magnetic particles and UV resin be controlled at 1:1 or lower for better patterning precision. In this paper, we use 1:1 as default mass ratio unless mentioned otherwise.

In this work, we mainly demonstrate the capability to pattern discrete 3D magnetization in planar materials, but this technique has potential to be extended to 3D structures due to the well-established DLP-based 3D printing technique. As a primary demonstration, Fig. 1C and Fig. 1D show a dual-layer structure patterned using a manual material feeding approach. The fabrication procedure for the dual-layer structure is described in **Error! Reference source not found.**.

Fig. 1. Schematic representation of the system for patterning discrete 3D magnetization. (**A**) Physical apparatus for patterning permanent magnetic particles in a UV-curable elastomeric matrix composite. (**B**) Experimentally measured maximum cross-link thickness with respect to magnetic particle concentration. Error bars indicate standard deviation. (**C**) Schematic representation of a dual-layer structure that has both horizontal and vertical magnetization components. Yellow arrows show the direction of magnetization patterned in each block. (**D**) Top view image of the dual-layer structure fabricated. Scale bar, 2 mm. (**E**) Out-of-plane magnetic flux distribution measured at the near surface of each layer separately using a magneto-optical sensor. The magneto-optical images are taken with the two layers fabricated independently to better visualize the magnetization profile.

Complex magnetic torque-induced deformation

Planar soft materials that have distributed 3D magnetization profiles can bend into pre-designed 3D shapes upon the application of a uniform magnetic field and return to the original shape once the field is removed. Fig. 2 and **Error! Reference source not found.** show the original states, actuating states, and schematic designs of different types of planar structures. Some of these untethered devices are patterned in a symmetric or centrosymmetric manner so that the net magnetization is in alignment with the external magnetic field during actuation, resulting in internal deformation rather than the rigid body rotation. As a general design rule, bending requires varying magnetization in the neutral axis plane (Fig. 2B-2C), while torsion requires magnetization perpendicular to the neutral axis (Fig. 2E). Structures that contain both parallel and normal magnetization components to the neutral axis yield a combined bending and torsion (Fig. 2F). Furthermore, advanced torque-induced deformation can be achieved by combing these design rules together. Higher-order bending (undulatory bending) is realized by patterning alternating magnetization segments, which generates pairs of counteracting magnetic torques (Fig. 2A and Fig. 2D). Large-angle (90°-180°) deflection is realized by the non-continuum transitions of magnetization angles in the plane of bending (Fig. 2G). By having multiple large-angle deflection structures, planar polymers can fold up to form a spherical hollow space in the center (Fig. 2H-2J). In Fig. 3A-3D, we provide simulation models to predict the shape changes. In Fig. 3E-3F, we show that different shape changes for the same tri-arm structure can be achieved by tuning the patterning angles. The capability to pattern arbitrary 3D magnetization and geometries allow highly deformable millimeter-scale structures under a magnetic field of 20 mT, which is readily available in a general electromagnetic coil system.

Fig. 2. Flexible magnetic planar structures that have distributed 3D magnetization profiles. Yellow arrows represent the direction of local magnetization and green arrows represent the direction of the actuating magnetic field. The materials are approximately 80 μm thick. The actuating magnetic field is 200 mT for "accordion" and less than 20 mT for all the others. All the items present reversible and rapid transformation between the original shape and the folding shape. Scale bars, 2 mm.

Fig. 3. Models for predicting the shape changes and capabilities to tune the patterning angle in 3D. (**A**) Side view images showing large-angle deflection under 20 mT. Scale bar, 2 mm. (**B**) Numerical model of the large-angle deflection. (**C**) Side view images showing undulatory bending of a ring under 20 mT. Scale bar, 2 mm. (**D**) Simulation of the ring using the finite element method. (**E**) Geometry, dimension, and the magnetization profile of the tri-arm structure. Unit, mm. (**F**) Top view images of the tri-arm structures that bear different magnetization profiles. They are actuated under a 20 mT magnetic field out of the plane. Scale bar, 2 mm.

Speed-tunable segmented magnetic swimmer

Magnetic microscale swimmers make use of corkscrew motion (*39*), beating flagellar motion (*40*, *41*), and traveling wave undulatory motion (*29*) for propulsion. Magnetic undulatory swimmers benefit from a simple structure, but the shape of the traveling wave in previous work cannot be tuned arbitrarily due to the continuous distribution of magnetization developed by template-aided magnetizing (*29*, *42*). Using the new patterning technique, we present undulatory swimmers that have the same size and volume magnetization but different magnetization pattern, resulting in different shape changes and swimming speeds under a rotating magnetic field. This arbitrary patterning method thus can serve as a versatile fabrication tool for studying underlying physical principles and creating optimized designs with tunable performance.

Fig. 4A, Fig. 4D, and **Error! Reference source not found.** show the designs of three types of swimmers fabricated from the same precursor. The swimming speed of each type of swimmer on the water surface was measured under different field strength and rotating frequencies (Fig. 4C). The theoretical swimming speed of each design is characterized using Traveling Wave Component (TWC) analysis (*42*), a method to evaluate the time-integral propulsive forces and the swimming speed of film-shaped undulatory swimmers. A detailed analysis is provided in **Error! Reference source not found.** and **Error! Reference source not found.**-S5. In Fig. 4B, the blue dots represent the theoretical deflection amplitude of the swimmers at each phase angle of the applied field, and the size of the equivalent circle serves as an indicator of the amplitude of the traveling wave and thus can serve as a heuristic for propulsive force of the swimmer in one period. The measured swimming speed data show a similar tendency to that of the simulated TWC analysis; type 1 design has an equivalent circle radius of 0.222 mm and thus the fastest swimming speed, followed by type 2 and type 3 design. In addition, the swimmers fabricated present high controllability in an electromagnetic coil system. Fig. 4E-4F and Movie S1 show a swimmer following an M-shaped path using a closed-loop vision feedback. With the surface tension of water surface restricting the movement along the Z-axis, heading of the swimmer can be controlled by changing the rotating axis of the driving magnetic field. The swimmer was actuated in a 9 mT rotating field at 20 Hz, presenting an average velocity of 3.38 mm/s (78.6% body length) and the maximum deviation of 0.2 mm (4.65 % body length).

Fig. 4. Millimeter-scale segmented magnetic swimmer. (**A**) Magnetization profiles of three types of swimmers. The body length L is 4.5 mm. (**B**) Simulated TWC analysis of the swimmers. Blue markers represent the deformation at each phase, while the yellow dashed lines represent the

equivalent deformation circle in one period. (**C**) Experimental swimming speed of the swimmers under different conditions. Solid triangles represent the average of six samples and error bars represent their standard deviations. (**D**) Segmented swimmers fabricated from the same precursor in one process. Scale bar, 1 mm. (**E**) Path following of a magnetic swimmer. (**F**) Path following error of a magnetic swimmer, corresponding to the path shown in **E**.

Multi-arm untethered magnetic microgripper

Grasping capability is among the most useful motions of microrobots, and the magnetically-actuated grippers have the advantages of being untethered and responsive. However, existing power grasping magnetic grippers can be fabricated only by manual assembly of magnetic components, which poses a great challenge to scaling and batch fabrication (*33*, *34*). Using the new method presented in this work, we achieve one-process fabrication of magnetic microgrippers that have configurable number of arms to target various cargos shapes (Fig. 5D). The fabrication time is also significantly decreased; it takes less than 20 minutes to fabricate one four-arm magnetic gripper, as opposed to 8 hours using the previous method (*34*) because of the manual assembly process (**Error! Reference source not found.**).

Fig. 5A shows the design of a magnetically actuated six-degree-of-freedom microgripper. Here, six actuated degrees of freedom refer to translation in three dimensions, pitch, yaw, and grasping motion. The microgripper consists of a base segment and several arms to enclose the cargo. Once the arms are folded, the gripper can be modeled as a rigid object and can locomote using rolling motion or the magnetic gradient pulling force. In Movie S1, we present the teleoperation of a microgripper as a mobile microrobot. Fig. 5B and Fig. 5C show the transportation of a green triangular prism-shaped PDMS cargo onto a 15˚ slope which simulates the terrain of unstructured environments. The cargo and the gripper began lying prone on the substrate in silicone oil. Then the gripper folded up and rolled toward the cargo under a rotating magnetic field. The gripper picked up the cargo using the pinching force at the tips, turned itself upside down, and secured the cargo using power grasping. Once it reached the target position, we reversed the direction of the magnetic field to release the cargo and rolled the gripper back to the home position.

Fig. 5. Untethered multi-arm magnetic microgripper. (**A**) Geometry, magnetization profile, and working mechanism of a magnetic microgripper. Black arrows represent the direction of local magnetization in each part, while blue arrows represent the actuating magnetic field. (**B**) Illustration of the cargo transportation task. (**C**) Top view and side view images of the cargo transportation task in silicone oil (20 cSt, Sigma-Aldrich). Silicone oil is used to lift the body weight and to slow down the shape changes of the gripper to make open-loop control easier. Scale bar, 5 mm. (**D**) Close-up images of different microgrippers at various field strength. Scale bar, 2 mm.

Multi-legged paddle-crawling robot

For small-scale robots, walking on a 2D surface requires breaking strong surface adhesion using techniques such as induced vibration (*43*), stick-slip-based motion (*44*), and surface engineering that provides superior adaptivity (*45*). From the perspective of motions, flexible magnetic microrobots typically crawl using inchworm motion, travelling wave motion (*31*), and continuous inverted-pendulum motion (*45*). Here, we show the paddle-crawling motion of a multi-legged robot under a rotating magnetic field. The walking gait of the robot is programmed by patterning alternating discrete magnetization in the legs.

Fig. 6A and Fig. 6B show the design and the locomotion mechanism of an eight-legged paddle-crawling robot. Bearing alternating magnetization in the legs, the robot can stand on legs

with body up and move forward using the stroke action under a rotating magnetic field. The stroke action involves the arms moving forward alternately with the legs kicking the ground throughout the stroke. Propulsive forces are generated by a combination of ground friction and fluid drag. Friction-based propulsion is dominant when the robot sinks to the bottom of the liquid while drag-based propulsion is dominant when the robot stays off the ground. Video of the paddle-crawling motion and the velocity of the multi-legged robot are presented in Movie S1 and **Error! Reference source not found.**. The robot bears an alternating magnetization along the body to make the net magnetization close to zero, which prevents the robot from somersaulting during lateral movement. The turning motion of the robot is presented in **Error! Reference source not found.**. Using a joystick controller, we can achieve controlled motion of the robot in a small confined microchannel (Fig. 6D-6E and Movie S1).

Fig. 6. Multi-legged paddle-crawling robot. (**A**) Image and magnetization profile of a paddle-crawling robot. Local magnetization is denoted by black arrows. When the legs labeled G1 perform power strokes, the legs labeled G2 perform recovery strokes, and vice versa. (**B**) Schematic representation of the gait from the side. (**C**) Top view images of the robot at different phases. (**D**) Illustration of the microchannel. The cross section of the channel is 4.7 mm × 1.0 mm. (**E**) Top view images showing the locomotion of the robot in a microchannel filled with silicone oil (20 cSt, Sigma-Aldrich). Silicone oil is used to lift the body weight and to slow down the stroke motions of the robot so that the camera can capture the motion clearly. The stroke motions and the velocity of the robot are faster in water. Scale bar, 4 mm.

Remote laser steering micromirror mount

UV curing allows direct printing of submillimeter-scale intricate features and tiny joints on a substrate without a microassembly process. With these tiny joints and patterned magnetization, we can fabricate untethered compact devices that have controllable minimal elastic deformations. To demonstrate this capability, we show a two-degree-of-freedom magnetic mirror mount that achieves high precision of motion.

Fig. 7A shows the design of an untethered mirror mount. The structure comprises a central stage for the mirror and four spring joints connected to the base. The tilting angle of the mirror can be controlled using a horizontal magnetic field, and it turns to the original position when the field is removed. To demonstrate the repeatability and accuracy, we performed an open-loop trajectory following experiment using a laser pointer in a coil system (Fig. 7B-7C). The reflected laser fell on the 20 mm × 20 mm region of a laser viewing card, and the position of the reflected laser was interpreted to the magnetic field using bilinear interpolation in the region of interest. We generated a time-varying magnetic field to draw a T-shaped trajectory and a star trajectory on the laser viewing card at 0.5 Hz and 0.2 Hz, respectively (Fig. 7D and Movie S1). The RMS accuracy (deviation from the desired trajectory) and the RMS precision (deviation from the mean trajectory) are summarized in Table 2. At frequencies higher than 0.5 Hz, the deviation from the desired trajectory becomes larger because of the momentum of the mirror.

Fig. 7. Untethered magnetic mirror mount for laser steering. (**A**) Close-up image of the mirror mount with a tiny mirror mounted at the center. The magnetization profile of the structure is shown in Fig. 2L. Scale bar, 2 mm. (**B**) Schematic representation of the laser steering experiment. (**C**) Coil system used in the experiment (*46*). (**D**) Target trajectories (orange) and experimental trajectories (blue) of the laser. The T-shaped and star-shaped trajectories are tracked at 0.5 and 0.2 Hz, respectively.

Table 2. Trajectory following results. Data were recorded with a 30 fps CMOS camera, each has no less than 10 cycles.

Trajectory	Frequency (Hz)	Path length (mm)	RMS accuracy (mm)	RMS precision (mm)
T	0.05	61	1.78 ± 2.46	0.10 ± 0.14
T	0.5	61	1.76 ± 2.42	0.10 ± 0.13
Star	0.05	72	1.72 ± 2.60	0.08 ± 0.11
Star	0.2	72	1.73 ± 2.49	0.62 ± 0.79

Magnetization Verification

The performance of a soft-bodied magnetic actuator depends on the precise patterning of magnetic particles. For example, the microgripper design in this paper requires 90° in the base block, -30° in the arm blocks, and -60° in the tip blocks to function properly. Here, we evaluate the patterning accuracy by viewing the distribution of the magnetic flux at sample surfaces using a magneto-optical sensor (Magview-S, Matesy GmbH). The measured data are compared with a magnetic dipole array-based model (**Error! Reference source not found.** and **Error! Reference source not found.**), in which we assume that the magnetic moment density in the material is uniform.

Fig. 8 shows the out-of-plane component of the magnetic flux 60 µm away from the sample surface. In Fig. 8A-8C, the measured magnetic flux density curves show good shape agreement with the model, demonstrating the capability of the proposed method to pattern the magnetization angles precisely. In Fig. 8E-8F, we magnetically encoded a QR code in a 5 mm × 5 mm region on a sheet of polymer. It shows that the precise magnetization feature size of 250 µm can be achieved using this technique, with clearly defined boundaries and sharp edges.

Fig. 8. Distribution of magnetic flux at the near surface of different samples. Modeled magnetic flux distribution, measured magnetic flux distribution, and the fitting results along the black dashed line of (**A**) a six-arm magnetic microgripper (front), (**B**) a six-arm magnetic microgripper (back), (**C**) an accordion, and (**D**) a multi-legged paddle-crawling robot. The data are collected 60 µm away from the sample surfaces. The magnitude of magnetization in the model is fitted to that in the measured data using least squares fitting. (**E**) Thin polymer sheet that carries a magnetically encoded QR code "UofT". Scale bar, 2 mm. (**F**) Magnetic flux measured at the surface of the QR code sample corresponding to **E**.

Discussion

In this work we developed a UV-lithography-based method for patterning permanent magnetic particles in planar composite materials, making it possible to fabricate actuators that have programmable 3D magnetization profiles, complex geometries, and thus new types of mechanical motions. This fabrication technique has potential to change the way we design and fabricate flexible microrobots; moreover, we can use it to extend the functionalities of existing miniaturized devices. Although we focus here on patterning magnetization in planar materials, our approach can be extended to 3D media using layer-by-layer curing, which is commonly used in stereolithography-based 3D printing. Multi-layer 3D architectures with programmable 3D magnetization profiles suggest new possibilities for applications in soft robotics and biomedical devices.

Typical stereolithography-based printing can achieve a feature size of several micrometers, but the theoretical feature size in the magnetic patterning method presented in this work is limited

by the size of the included permanent magnetic particles (5 μm in this work). The assumption of homogeneous magnetic moment density does not hold if the size of individual magnetization area begins to approach the scale of the particles; in addition, because the particle size imposes a limit to the thickness of the fabricated product, the microrobots cannot be scaled down arbitrarily small even if the assumption is valid. In practice, considering the particle size distribution and irregular particle shapes, we recommend the magnetization feature size roughly one order of magnitude bigger than the particle size to maintain reasonably homogeneous magnetic moment density.

Biocompatibility is also a critical factor for successful application in biomedical use. In this work, the NdFeB permanent magnetic particles are securely encased by cured polymer composites, so the particles are not in direct contact with the environment to harm biological tissue. In addition, the patterning technique is transferrable to most UV curing polymers, so different encasement materials can be chosen according to the temperature and acidity of the working environment to ensure safety. To reduce heavy metal toxicity, samarium cobalt or ferrite permanent magnetic particles can be substituted for NdFeB magnetic particles. Typical use of small-scale robots in biological application inside the human body would require removal from the body upon completion of their tasks for safer robot-animal interaction.

Materials and Methods

Preparation of materials

Permanent magnetic particles that have an average diameter of 5 μm (MQFP-15-7, NdFeB, Magnequench) were pre-magnetized in a 1.1 T uniform magnetic field between two N52 one-inch permanent magnets with a 3 mm gap. Acquiring saturation remanence, the magnetic particles were mixed sufficiently with UV resin (DLP/SLA 3D Printer UV Resin, Flexible Type, GC3D-EBE) in a mass ratio of 1:1 to form a homogeneous magnetic slurry. To ensure particle dispersion, we prepare 0.5 g magnetic slurry on a glass slide and use a glass rod to stir it constantly for 3 min. The magnetic slurry is placed in a vacuum degassing chamber for 1 min to remove the bubbles. Then the magnetic slurry is loaded into a negative SU8 mold (6 mm × 6 mm × 0.08 mm) prepared using photolithography. The thickness of the SU8 photoresist layer determines the thickness of the final product. The magnetic slurry is covered by a No.1 microscope coverslip (22 mm × 22 mm × 0.15 mm) and the substrate is mounted to the center of the fabrication stage.

Physical apparatus

Fig. 1A and **Error! Reference source not found.** show the physical apparatus for patterning magnetic particles in UV resin. The apparatus consists of a DLP-based lithography system and a magnetic field generator. They are controlled by a computer for automating the fabrication process. A detailed schematic diagram of the hardware connection and signal flow is in **Error! Reference source not found.** and **Error! Reference source not found.**.

The DLP-based lithography system comprises a UV DLP projector (Texas Instruments DLP Lightcrafter 4500, modified with a 405 nm light engine), a plano-convex lens (N-BK7, Ø50.8 mm, f = 75.0 mm, Thorlabs), two cube-mounted non-polarizing beamsplitters, a Nikon 10x/0.30A microscope objective lens, and a vertical precision stage. A CMOS camera is installed above the beamsplitter, vertically aligned with the objective lens and the fabrication stage for focus adjustment. With a digital micromirror array in the DLP projector serving as a photomask, the binary image generated by the computer passes through the projector aperture, the plano-convex lens, and the objective lens, forming a demagnified image in the workspace (approximately 6.0 mm

× 6.0 mm) on the object plane. The height of the fabrication stage can be adjusted by the vertical precision knob to bring the object image into focus.

The magnetic field generator comprises an N52 one-inch permanent magnet, two stepper motors, and a 3-axis magnetic field sensor (TLV493D-A1B6, DigiKey). The permanent magnet is held in a way that the center of the magnet is fixed but the azimuthal and polar angles can be independently controlled by two motors. The permanent magnet is placed 4.5 cm under the fabrication stage so that it generates 80 mT to 160 mT magnetic flux density in the workspace area, depending on the magnet orientation. We assume that the direction and the strength of the magnetic field in this area are nearly uniform. Based on the magnetic dipole model and the feedback data from the 3-axis magnetic field sensor, we can generate a magnetic field to precisely reorient the pre-magnetized particles in the slurry and bring them into alignment with any 3D direction.

In its current state, the proposed patterning system has two major problems. First, the size of the permanent magnet limits the size of the workspace because the magnetic field used to reorient the particles is no longer uniform if the size of the workspace is increased. Second, the fabrication stage is not motorized, so it can only pattern magnetization in planar materials. In **Error! Reference source not found.**, we introduce a manual material feeding approach for multi-layer patterning and discuss how the physical apparatus can be further improved.

Fabrication Procedure

The substrate is placed at the center of the fabrication stage, vertically aligned with the objective lens and the magnetic field sensor. Patterning of local magnetization involves two steps: reorientation of included magnetic particles and selective curing of UV resin. First, the stepper motors orient the permanent magnet to generate the desired magnetic field, which reorients all the pre-magnetized magnetic particles in the magnetic slurry. Once the motors reach the desired configuration, both motors perform a damped oscillation that has an initial amplitude of 15° to bring the particles into alignment faster. After allowing 2 min for particle reorientation, UV light shines on selected regions of the magnetic slurry, initiating polymerization and freezing the magnetic particles within that area. For UV curing, we run the LED of the DLP projector (Texas Instruments DLP Lightcrafter 4500, modified with a 405 nm light engine) for 1.5 sec at 62.74% PWM duty cycle, which corresponds to 2.71 A current and 80 lx illuminance according to the datasheet. The two steps are repeated optionally until all the regions are patterned and cured properly. Movie S1 shows the fabrication procedure of the two-arm gripper presented in Fig. 2G.

Optical system characterization

We used a beam profiler (UV-Spiricon Ophir, BGP-USB-SP928-OSI) to evaluate the geometrical resolution of the UV light on the object plane. We generated squares of various sizes at the object plane and measured the intensity profiles. In the current configuration of optical components, the system has the geometrical feature size as small as 100 μm × 100 mm on the object plane, according to the 10/90 edge-steepness metric (**Error! Reference source not found.** and **Error! Reference source not found.**-S13). The geometrical resolution at the object plane, however, can be increased at the cost of reducing the size of the workspace area by selecting optical components with a higher magnification.

Strength of the magnetic field applied when curing

In the proposed method, local magnetization is patterned by reorienting the pre-magnetized particles and then curing the resin with UV light. In the physical reorientation process, viscous drag

in the UV resin is the principle effect that hinders particle reorientation. Increasing field strength (but not strong enough to magnetize the particles) or present time in the field can both bring more particles into perfect alignment, resulting in stronger magnetization after curing. In a preliminary study (**Error! Reference source not found.**), we conducted a controlled experiment to investigate the influence of field strength on resulting magnetization. The results show that field strength of 80 mT and present time for 2 min can produce about 75% resulting magnetization compared with that of saturated samples.

Models to predict the shape changes

Finite element analysis is used to predict the shape changes of the materials that have a small deformation. In these models, we used a static structural module in ANSYS with the assumption that the materials have isotropic mechanical property. Young's modulus E = 331.8 kPa (UV resin cured using 405 nm blue light with illuminance of 80 lx, exposure time 1.5 s, **Error! Reference source not found.** and **Error! Reference source not found.**), Poisson's ratio ν = 0.49, magnetization M = 24kA/m (pre-magnetized NdFeB powders and UV resin in a mass ratio of 1:1) are used. For large-angle deflection, we used a custom MATLAB script that conceptually divides the materials into an array of tiny elements, each of which contains a magnetic dipole. The deflection of each element is modeled using Euler-Bernoulli beam theory. The numerical model goes through several iterations until the equilibrium state is reached.

Electromagnetic coil system used for actuation

In this paper, we use a custom Helmholtz electromagnetic coil system for actuating the microrobots unless noted otherwise. **Error! Reference source not found.** shows the image of the coil system. Each coil is powered by an individual amplifier (ADVANCED Motion Controls, 30A8, maximum 15 A continuous current) and controlled by the analog output of a multifunction analog/digital I/O board (Sensoray, Model 826). It can generate a uniform magnetic field up to 20 mT in any direction, and up to 50 Hz without a significant drop in field strength. The measured workspace area is approximately 2.0 cm × 5.5 cm × 4.5 cm.

SUPPLEMENTARY MATERIALS

Text S1. Manual material feeding for multi-layer structures.
Text S2. TWC (Travelling Wave Component) analysis for magnetic swimmers.
Text S3. Time required for fabricating a four-arm magnetic gripper.
Text S4. Velocity of multi-legged paddle-crawling robot.
Text S5. Turning motion of multi-legged paddle-crawling robot.
Text S6. Magnetic dipole array model for calculating the distribution of magnetic flux.
Text S7. Connection of hardware and flow of control signals.
Text S8. Geometrical resolution of the custom UV-lithography system.
Text S9. Measurement of Young's modulus of the material.
Text S10. Magnitude of the magnetization developed by reorienting pre-magnetized particles.
Fig. S1. Sequence diagram for patterning magnetization in a dual-layer structure.
Fig. S2. Magnetization and dimensions of the devices fabricated.
Fig. S3. TWC analysis of the deformation of type 1 swimmer at different magnetic field angles.
Fig. S4. TWC analysis of the deformation of type 2 swimmer at different magnetic field angles.
Fig. S5. TWC analysis of the deformation of type 3 swimmer at different magnetic field angles.
Fig. S6. Velocity of the multi-legged robot crawling in silicone oil under a 1Hz rotating magnetic field.
Fig. S7. Velocity of the multi-legged robot swimming (drag-based paddling) at the interface of water and silicone oil under a 2Hz rotating magnetic field.
Fig. S8. Schematic representation of steering motion of the multi-legged paddle-crawling robot.
Fig. S9. Schematic representation of the magnetic dipole array model.
Fig. S10. Image of the physical apparatus.

Fig. S11. Schematic representation of signal flow and hardware control.
Fig. S12. Intensity profile of squares generated at the object plane.
Fig. S13. Intensity profile of other shapes generated at the object plane.
Fig. S14. Measurement of the stiffness of the material using microforce sensor.
Fig. S15. Electromagnetic coil system used for actuation.
Fig. S16. Distribution of magnetic flux observed at the near surface of the samples cured in different field strength.
Table S1. Dimension, magnetization, and parameters obtained from TWC analysis.
Table S2. Coefficient of first-order terms of the Fourier series in TWC analysis.
Table S3. Dimensions of the sample used in Young's modulus measurement.
Movie S1 (.mp4 format). Fabrication procedure and demonstration of the microrobots.

REFERENCE AND NOTES

1. B. J. Nelson, I. K. Kaliakatsos, J. J. Abbott, Microrobots for Minimally Invasive Medicine. *Annu. Rev. Biomed. Eng.* **12**, 55–85 (2010).
2. H. Ceylan, J. Giltinan, K. Kozielski, M. Sitti, Mobile microrobots for bioengineering applications. *Lab Chip* **17**, 1705–1724 (2017).
3. D. Cappelleri, D. Efthymiou, A. Goswami, N. Vitoroulis, M. Zavlanos, Towards mobile microrobot swarms for additive micromanufacturing. *Int. J. Adv. Robot. Syst.* **11**, 9 (2014).
4. J. Li, B. Esteban-Fernández de Ávila, W. Gao, L. Zhang, J. Wang, Micro/nanorobots for biomedicine: Delivery, surgery, sensing, and detoxification. *Sci. Robot.* **2**, eaam6431 (2017).
5. H. McClintock, F. Z. Temel, N. Doshi, J.-S. Koh, R. J. Wood, The milliDelta: A high-bandwidth, high-precision, millimeter-scale Delta robot. *Sci. Robot.* **3**, eaar3018 (2018).
6. A. T. Baisch, O. Ozcan, B. Goldberg, D. Ithier, R. J. Wood, High speed locomotion for a quadrupedal microrobot. *Int. J. Rob. Res.* **33**, 1063–1082 (2014).
7. A. Ghosh, C. Yoon, F. Ongaro, S. Scheggi, F. M. Selaru, S. Misra, D. H. Gracias, Stimuli-Responsive Soft Untethered Grippers for Drug Delivery and Robotic Surgery. *Front. Mech. Eng.* **3**, 7 (2017).
8. J. Randhawa, T. Leong, N. Bassik, B. Benson, M. Jochmans, D. Gracias, Pick-and-place using chemically actuated microgrippers. *J. Am. Chem. Soc.* **130**, 17238–17239 (2008).
9. A. Nojoomi, H. Arslan, K. Lee, K. Yum, Bioinspired 3D structures with programmable morphologies and motions. *Nat. Commun.* **9**, 1–11 (2018).
10. J. Li, I. Rozen, J. Wang, Rocket Science at the Nanoscale. *ACS Nano* **10**, 5619–5634 (2016).
11. F. Soto, A. Martin, S. Ibsen, M. Vaidyanathan, V. Garcia-Gradilla, Y. Levin, A. Escarpa, S. C. Esener, J. Wang, Acoustic microcannons: Toward advanced microballistics. *ACS Nano* **10**, 1522–1528 (2016).
12. D. Ahmed, M. Lu, A. Nourhani, P. E. Lammert, Z. Stratton, H. S. Muddana, V. H. Crespi, T. J. Huang, Selectively manipulable acoustic-powered microswimmers. *Sci. Rep.* **5**, 9744 (2015).
13. M. J. Villangca, D. Palima, A. R. Bañas, J. Glückstad, Light-driven micro-tool equipped with a syringe function. *Light Sci. Appl.* **5**, e16148 (2016).
14. W. Hu, K. S. Ishii, Q. Fan, A. T. Ohta, Hydrogel microrobots actuated by optically generated vapour bubbles. *Lab Chip* **12**, 3821–3826 (2012).
15. X. Yan, Q. Zhou, M. Vincent, Y. Deng, J. Yu, J. Xu, T. Xu, T. Tang, L. Bian, Y.-X. J. Wang, K. Kostarelos, L. Zhang, Multifunctional biohybrid magnetite microrobots for imaging-guided therapy. *Sci. Robot.* **2**, eaaq1155 (2017).
16. C. Peters, M. Hoop, S. Pané, B. J. Nelson, C. Hierold, Degradable Magnetic Composites for Minimally Invasive Interventions: Device Fabrication, Targeted Drug Delivery, and Cytotoxicity Tests. *Adv. Mater.* **28**, 533–538 (2016).
17. U. Bozuyuk, O. Yasa, I. C. Yasa, H. Ceylan, S. Kizilel, M. Sitti, Light-Triggered Drug Release from 3D-Printed Magnetic Chitosan Microswimmers. *ACS Nano* **12**, 9617–9625 (2018).
18. T. Y. Huang, M. S. Sakar, A. Mao, A. J. Petruska, F. Qiu, X. B. Chen, S. Kennedy, D. Mooney, B. J. Nelson, 3D Printed Microtransporters: Compound Micromachines for Spatiotemporally Controlled Delivery of Therapeutic Agents. *Adv. Mater.* **27**, 6644–6650 (2015).
19. A. Servant, F. Qiu, M. Mazza, K. Kostarelos, B. J. Nelson, Controlled in vivo swimming of a swarm of bacteria-like microrobotic flagella. *Adv. Mater.* **27**, 2981–2988 (2015).
20. X. Yan, Q. Zhou, J. Yu, T. Xu, Y. Deng, T. Tang, Q. Feng, L. Bian, Y. Zhang, A. Ferreira, L. Zhang, Magnetite Nanostructured Porous Hollow Helical Microswimmers for Targeted Delivery.

Adv. Funct. Mater. **25**, 5333–5342 (2015).

21. S. Kim, F. Qiu, S. Kim, A. Ghanbari, C. Moon, L. Zhang, B. J. Nelson, H. Choi, Fabrication and characterization of magnetic microrobots for three-dimensional cell culture and targeted transportation. *Adv. Mater.* **25**, 5863–5868 (2013).

22. M. Medina-Sánchez, L. Schwarz, A. K. Meyer, F. Hebenstreit, O. G. Schmidt, Cellular Cargo Delivery: Toward Assisted Fertilization by Sperm-Carrying Micromotors. *Nano Lett.* **16**, 555–61 (2016).

23. I. S. M. Khalil, D. Mahdy, A. El Sharkawy, R. R. Moustafa, A. F. Tabak, M. E. Mitwally, S. Hesham, N. Hamdi, A. Klingner, A. Mohamed, M. Sitti, Mechanical Rubbing of Blood Clots Using Helical Robots Under Ultrasound Guidance. *IEEE Robot. Autom. Lett.* **3**, 1112–1119 (2018).

24. C. Hu, S. Pané, B. J. Nelson, Soft Micro- and Nanorobotics. *Annu. Rev. Control. Robot. Auton. Syst.* **1**, 53–75 (2018).

25. J. Kudr, Y. Haddad, L. Richtera, Z. Heger, M. Cernak, V. Adam, O. Zitka, Magnetic Nanoparticles: From Design and Synthesis to Real World Applications. *Nanomaterials* **7**, 243–271 (2017).

26. H. W. Huang, M. S. Sakar, A. J. Petruska, S. Pané, B. J. Nelson, Soft micromachines with programmable motility and morphology. *Nat. Commun.* **7**, 12263 (2016).

27. J. Kim, S. E. Chung, S. E. Choi, H. Lee, J. Kim, S. Kwon, Programming magnetic anisotropy in polymeric microactuators. *Nat. Mater.* **10**, 747–752 (2011).

28. D. Kokkinis, M. Schaffner, A. R. Studart, Multimaterial magnetically assisted 3D printing of composite materials. *Nat. Commun.* **6**, 8643 (2015).

29. E. Diller, J. Zhuang, G. Zhan Lum, M. R. Edwards, M. Sitti, Continuously distributed magnetization profile for millimeter-scale elastomeric undulatory swimming. *Appl. Phys. Lett.* **104**, 174101 (2014).

30. G. Z. Lum, Z. Ye, X. Dong, H. Marvi, O. Erin, W. Hu, M. Sitti, Shape-programmable magnetic soft matter. *Proc. Natl. Acad. Sci.* **113**, E6007–E6015 (2016).

31. W. Hu, G. Z. Lum, M. Mastrangeli, M. Sitti, Small-scale soft-bodied robot with multimodal locomotion. *Nature* **554**, 81–85 (2018).

32. S. Tasoglu, E. Diller, S. Guven, M. Sitti, U. Demirci, Untethered micro-robotic coding of three-dimensional material composition. *Nat. Commun.* **5**, 3124 (2014).

33. E. Diller, M. Sitti, Three-dimensional programmable assembly by untethered magnetic robotic micro-grippers. *Adv. Funct. Mater.* **24**, 4397–4404 (2014).

34. J. Zhang, O. Onaizah, K. Middleton, L. You, E. Diller, Reliable Grasping of Three-Dimensional Untethered Mobile Magnetic Microgripper for Autonomous Pick-and-Place. *IEEE Robot. Autom. Lett.* **2**, 835–840 (2017).

35. Y. Kim, H. Yuk, R. Zhao, S. A. Chester, X. Zhao, Printing ferromagnetic domains for untethered fast-transforming soft materials. *Nature* **558**, 274–279 (2018).

36. R. Dreyfus, J. Baudry, M. L. Roper, M. Fermigier, H. A. Stone, J. Bibette, Microscopic artificial swimmers. *Nature* **437**, 862–865 (2005).

37. T. Qiu, T. C. Lee, A. G. Mark, K. I. Morozov, R. Münster, O. Mierka, S. Turek, A. M. Leshansky, P. Fischer, Swimming by reciprocal motion at low Reynolds number. *Nat. Commun.* **5**, 5119 (2014).

38. Z. Z. Bandic, R. H. Victora, Advances in magnetic data storage technologies. *Proc. IEEE* **96**, 1749–1753 (2008).

39. S. Tottori, L. Zhang, F. Qiu, K. K. Krawczyk, A. Franco-Obregón, B. J. Nelson, Magnetic Helical Micromachines: Fabrication, Controlled Swimming, and Cargo Transport. *Adv. Mater.* **24**, 811–816 (2012).

40. A. M. Maier, C. Weig, P. Oswald, E. Frey, P. Fischer, T. Liedl, Magnetic Propulsion of Microswimmers with DNA-Based Flagellar Bundles. *Nano Lett.* **16**, 906–910 (2016).

41. I. S. M. Khalil, A. F. Tabak, Y. Hamed, M. E. Mitwally, M. Tawakol, A. Klingner, M. Sitti, Swimming Back and Forth Using Planar Flagellar Propulsion at Low Reynolds Numbers. *Adv. Sci.* **5**, 1700461 (2018).

42. J. Zhang, E. Diller, Untethered Miniature Soft Robots: Modeling and Design of a Millimeter-Scale Swimming Magnetic Sheet. *Soft Robot.* **5**, 761–776 (2018).

43. W. Jing, X. Chen, S. Lyttle, Z. Fu, Y. Shi, D. J. Cappelleri, paper presented at IEEE International Conference on Robotics and Automation, Shanghai, China, 10 May 2011.

44. C. Pawashe, S. Floyd, M. Sitti, Modeling and experimental characterization of an untethered magnetic micro-robot. *Int. J. Rob. Res.* **28**, 1077–1094 (2009).

45. H. Lu, M. Zhang, Y. Yang, Q. Huang, T. Fukuda, Z. Wang, Y. Shen, A bioinspired multilegged soft millirobot that functions in both dry and wet conditions. *Nat. Commun.* **9**, 1–7 (2018).

46. S. Salmanipour, E. Diller, paper presented at IEEE International Conference on Robotics and Automation, Brisbane, QLD, 21-25 May 2018.

Acknowledgments

Acknowledgements: We thank Shuailong Zhang in Wheeler Microfluidics Laboratory lab in University of Toronto for his assistance in the optical system design.

Funding: Support for this project was provided by the Natural Sciences and Engineering Research Council of Canada through the Discovery Grant Program grant #2014-04703.

Data and materials availability: All data needed to evaluate the conclusions in the paper are present in the paper or the Supplementary Materials. The code used to control the coil system is available under the MIT License at https://github.com/atelier-ritz/CoilSystemPython. The code used to pattern the magnetic particles is available under the MIT license at https://github.com/atelier-ritz/pycrafter4500_stepper-based.

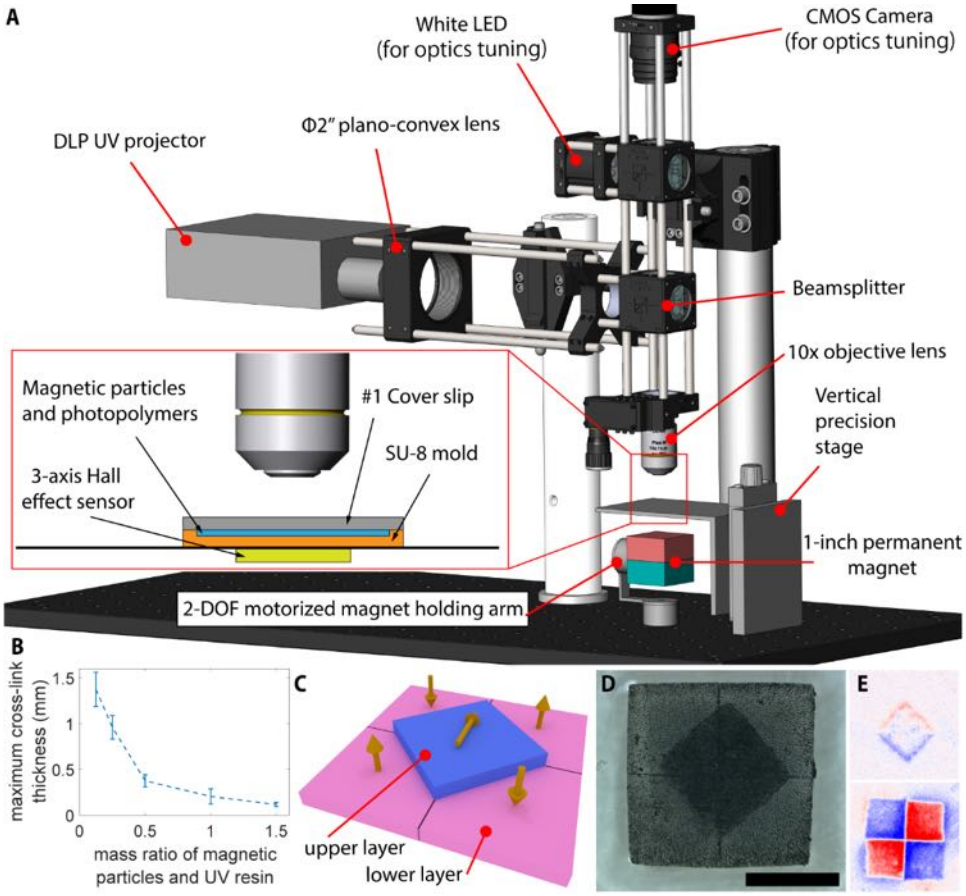

Fig. 1. Schematic representation of the system for patterning discrete 3D magnetization. (**A**) Physical apparatus for patterning permanent magnetic particles in a UV-curable elastomeric matrix composite. (**B**) Experimentally measured maximum cross-link thickness with respect to magnetic particle concentration. (**C**) Schematic representation of a dual-layer structure that has both horizontal and vertical magnetization components. (**D**) Top view image of the dual-layer structure fabricated. Scale bar, 2 mm. (**E**) Out-of-plane magnetic flux distribution measured at the near surface of each layer using a magneto-optical sensor. The images are taken with the two layers detached.

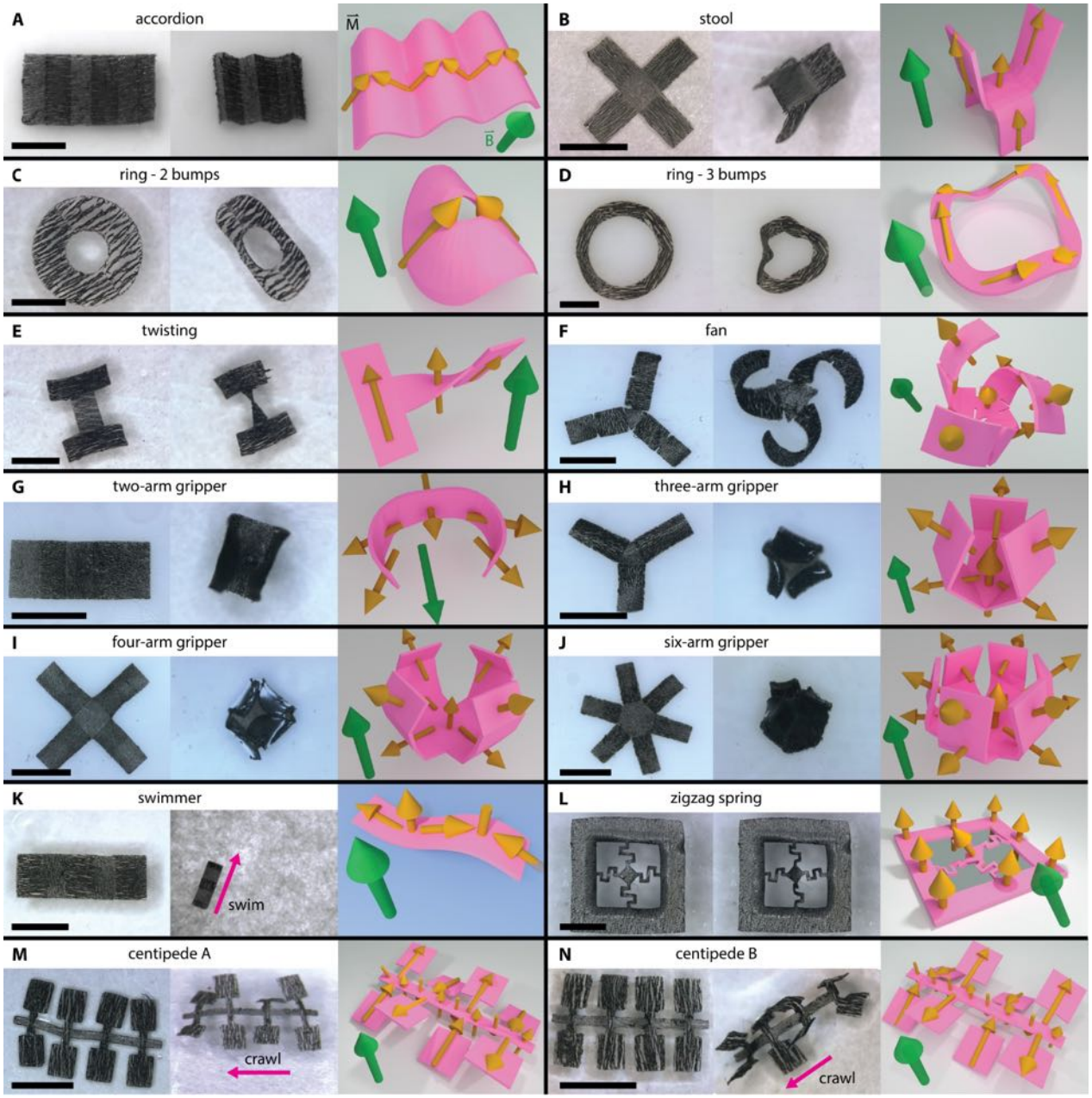

Fig. 2. Flexible magnetic planar structures that have distributed 3D magnetization profiles. Yellow arrows represent the direction of local magnetization and green arrows represent the direction of the actuating magnetic field. The materials are approximately 80 μm thick. The actuating magnetic field is 200 mT for "accordion" and less than 20 mT for all the others. All the items present reversible and rapid transformation between the original shape and the folding shape. Scale bars, 2 mm.

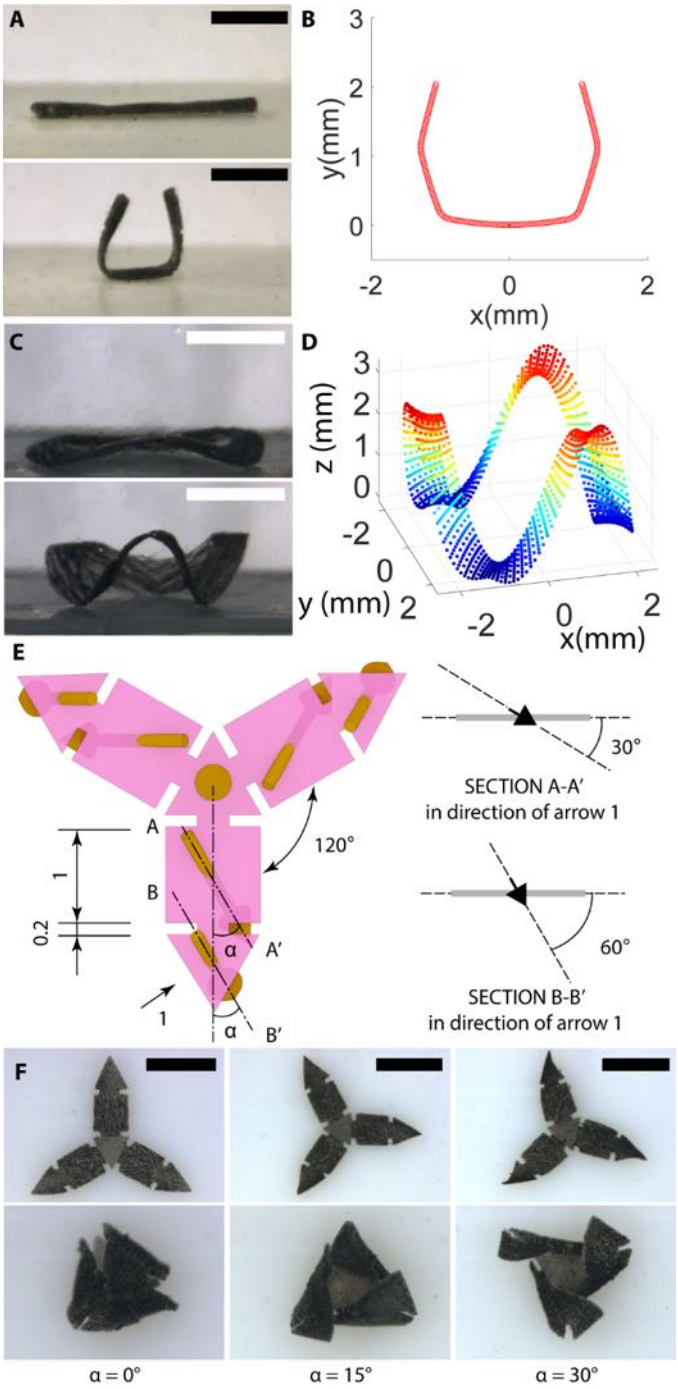

Fig. 3. Models for predicting the shape changes and capabilities to tune the patterning angle in 3D. (**A**) Side view images showing large-angle deflection under 20 mT. Scale bar, 2 mm. (**B**) Numerical model of the large-angle deflection. (**C**) Side view images showing undulatory bending of a ring under 20 mT. Scale bar, 2 mm. (**D**) Simulation of the ring using the finite element method. (**E**) Geometry, dimension, and the magnetization profile of the tri-arm structure. Unit, mm. (**F**) Top view images of the tri-arm structures that bear different magnetization profiles. They are actuated under a 20 mT magnetic field out of the plane. Scale bar, 2 mm.

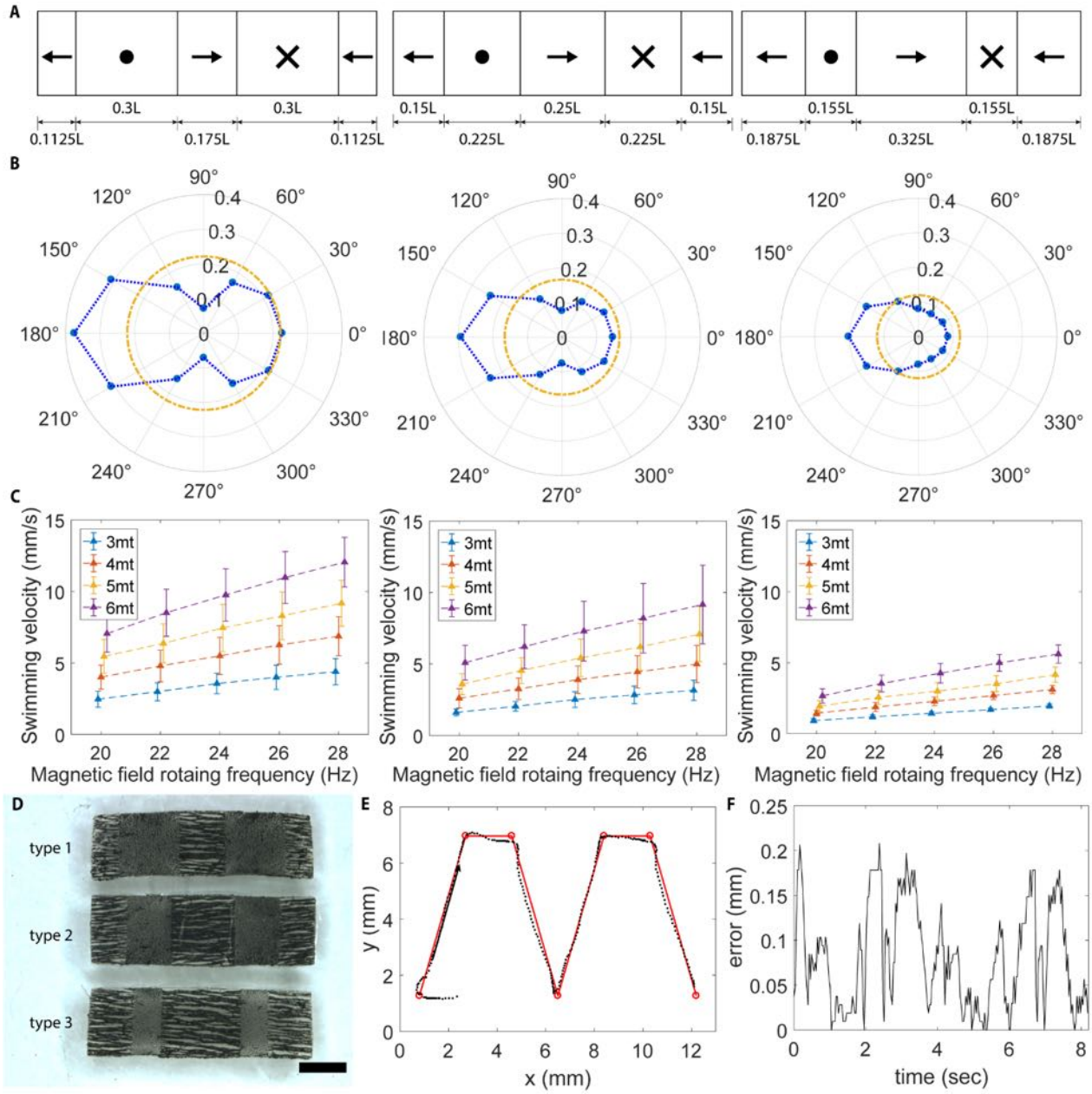

Fig. 4. Millimeter-scale segmented magnetic swimmer. (**A**) Magnetization profiles of three types of swimmers. The body length L is 4.5 mm. (**B**) Simulated TWC analysis of the swimmers. Blue markers represent the deformation at each phase, while the yellow dashed lines represent the equivalent deformation circle in one period. (**C**) Experimental swimming speed of the swimmers under different conditions. Solid triangles represent the average of six samples and error bars represent their deviations. (**D**) Segmented swimmers fabricated from the same precursor in one process. Scale bar, 1 mm. (**E**) Path following of a magnetic swimmer. (**F**) Path following error of a magnetic swimmer, corresponding to the path shown in **E**.

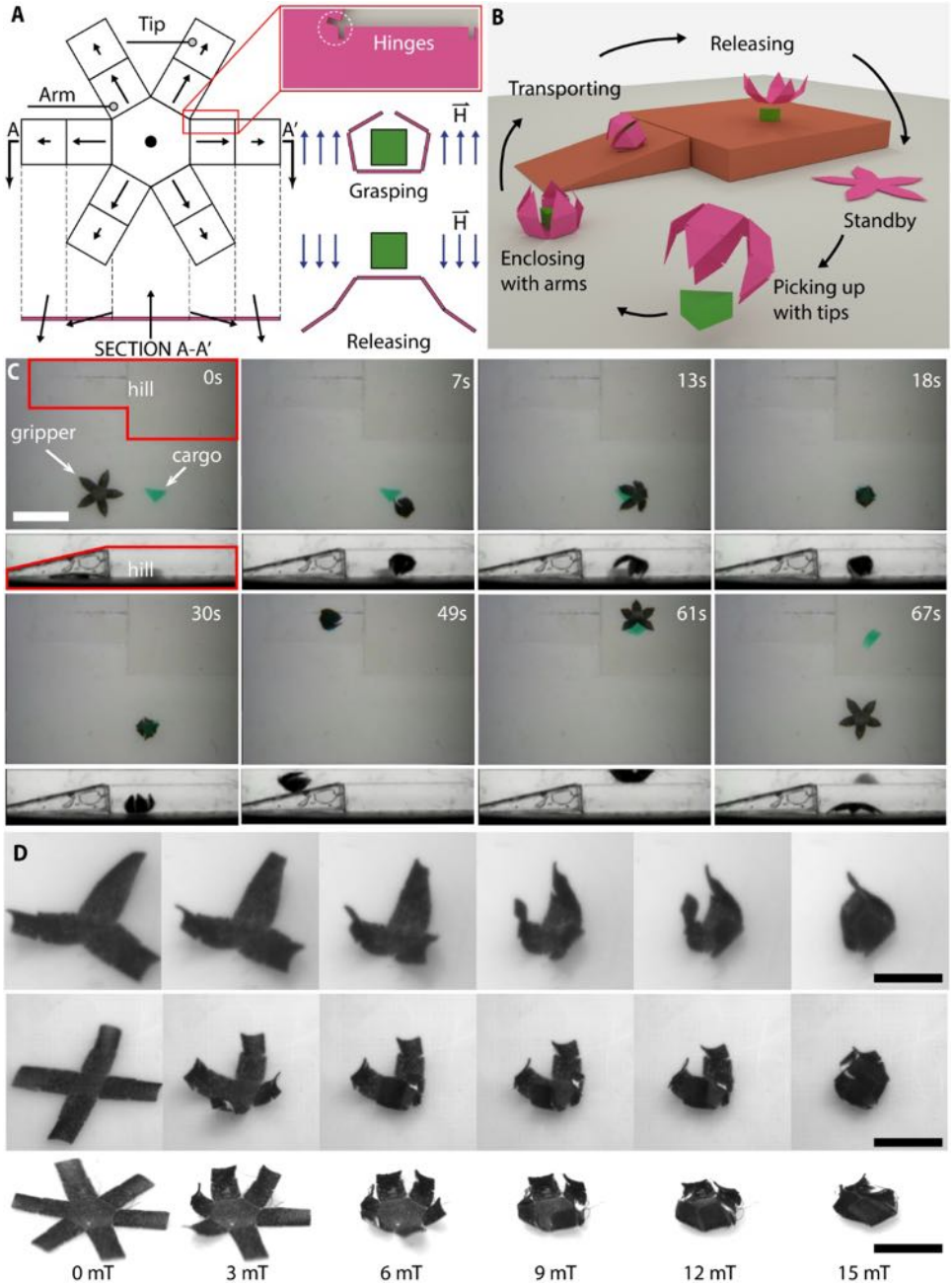

Fig. 5. Untethered multi-arm magnetic microgripper. (**A**) Geometry, magnetization profile, and working mechanism of a magnetic microgripper. Black arrows represent the direction of local magnetization in each part, while blue arrows represent the actuating magnetic field. (**B**) Illustration of the cargo transportation task. (**C**) Top view and side view images of the cargo transportation task in silicone oil (20 cSt, Sigma-Aldrich). Silicone oil is used to lift the body weight and to slow down the shape changes of the gripper to make open-loop control easier. Scale bar, 5 mm. (**D**) Close-up images of different microgrippers at various field strength. Scale bar, 2 mm.

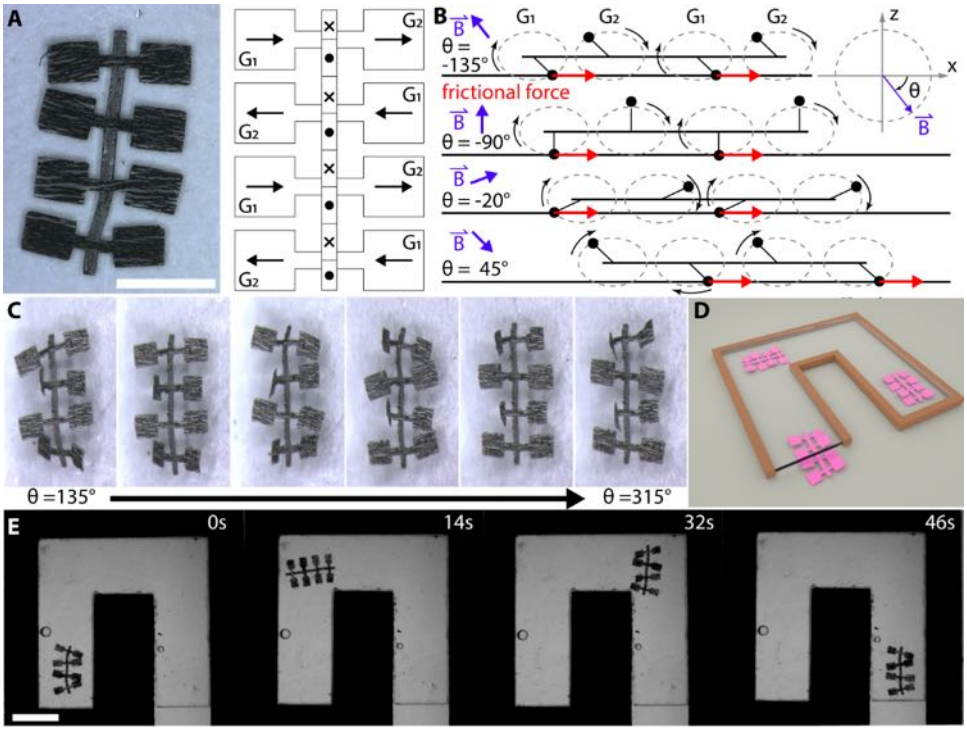

Fig. 6. Multi-legged paddle-crawling robot. (**A**) Image and magnetization profile of a paddle-crawling robot. Local magnetization is denoted by black arrows. When the legs labeled G1 perform power strokes, the legs labeled G2 perform recovery strokes, and vice versa. (**B**) Schematic representation of the gait from the side. (**C**) Top view images of the robot at different phases. (**D**) Illustration of the microchannel. The cross section of the channel is 4.7 mm × 1.0 mm. (**E**) Top view images showing the locomotion of the robot in a microchannel filled with silicone oil (20 cSt, Sigma-Aldrich). Silicone oil is used to life the body weight and to slow down the stroke motions of the robot so that the camera can capture the motion clearly. The stroke motions and the velocity of the robot are faster in water. Scale bar, 4 mm.

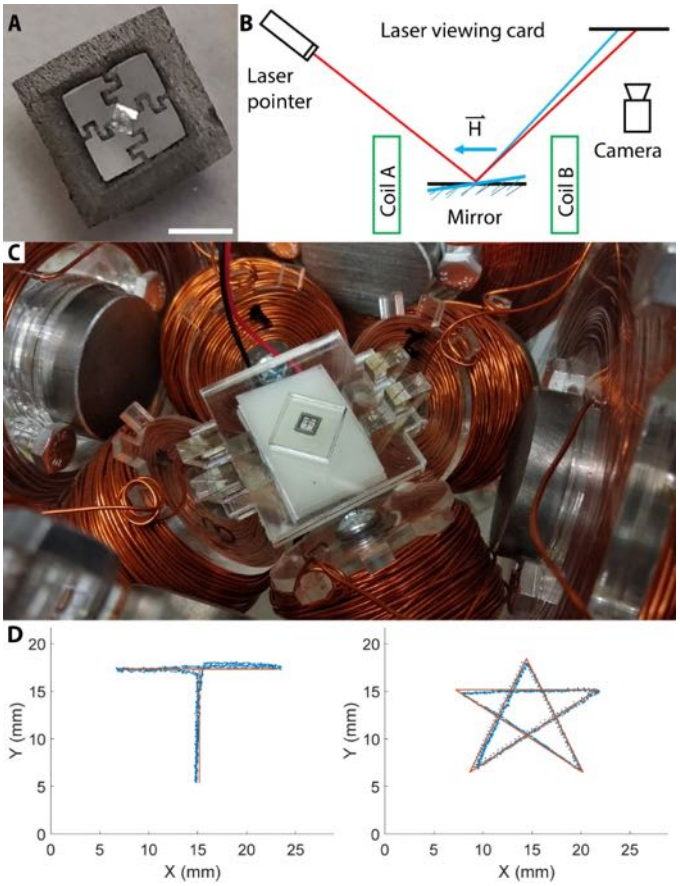

Fig. 7. Untethered magnetic mirror mount for laser steering. (**A**) Close-up image of the mirror mount with a tiny mirror mounted at the center. The mirror is mounted on the structure in Fig. 2L. Scale bar, 2 mm. (**B**) Schematic representation of the laser steering experiment. (**C**) Coil system used in the experiment (*46*). (**D**) Target trajectories (orange) and experimental trajectories (blue) of the laser. The T-shaped and star-shaped trajectories are tracked at 0.5 and 0.2 Hz, respectively.

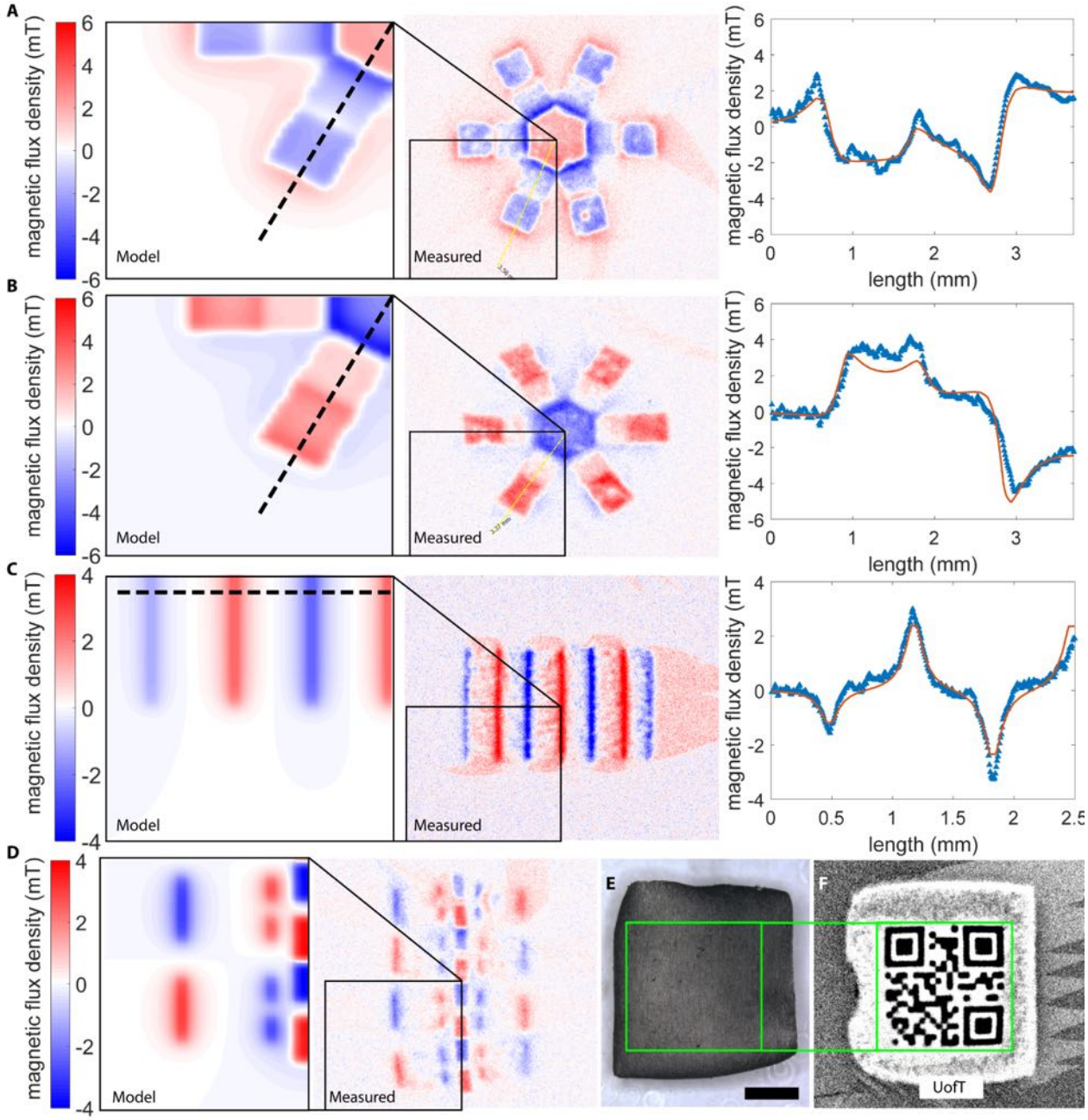

Fig. 8. Distribution of magnetic flux at the near surface of different samples. Modeled magnetic flux distribution, measured magnetic flux distribution, and the fitting results along the black dashed line of (**A**) a six-arm magnetic microgripper (front), (**B**) a six-arm magnetic microgripper (back), (**C**) an accordion, and (**D**) a multi-legged paddle-crawling robot. The data are collected 60 μm away from the sample surfaces. The magnitude of magnetization in the model is fitted to that in the measured data using least squares fitting. (**E**) Thin polymer sheet that carries the magnetically encoded QR code "UofT". Scale bar, 2 mm. (**F**) Magnetic flux measured at the surface of the QR code sample corresponding to **E**.